RADBOUD UNIVERSITEIT NIJMEGEN

FACULTEIT DER NATUURWETENSCHAPPEN, WISKUNDE EN INFORMATICA

Dwarf Galaxies and Dark Matter

DETERMINING THE DARK MATTER CONTENT OF DWARF GALAXIES BY MEANS OF JEANS ANALYSIS

BACHELOR'S THESIS PHYSICS AND ASTRONOMY

Supervisor:
dr. Sascha CARON

Author:
Eric Teunis DE BOONE

Second Reader:
prof. Jörg HÖRANDEL

December 2019

Contents

1. Introduction

Since 1933 there is information on discrepancies between the theories for gravity and both the luminosity of galaxies and larger structures in the universe. Over time, more pointers have been found, indicating that all that we see is not all there is.

In the current Standard Model of Cosmology (ΛCDM), 70% of the universe's mass-energy is Dark Energy (the Λ), 25% is (cold) Dark Matter (the CDM), with the rest being the 'visible' matter and energy. The nature of Dark Matter (DM) is presumed to be very limited in electromagnetic interactions, explaining the non-observability by telescopes.

To explore this nature, multiple theories and experiments have been put forward.

1.1 Clues for Dark Matter

A hint to a 'missing mass' was found in rotation curves of galaxies. The rotational velocity within such a galaxy does not fall off with increasing radius in a manner that Newtonian Dynamics suggests. Instead, it falls off very slowly as if there is additional mass which had not been taken into account. In Figure 1.1a, the difference between the observed and expected velocity curves can be observed.
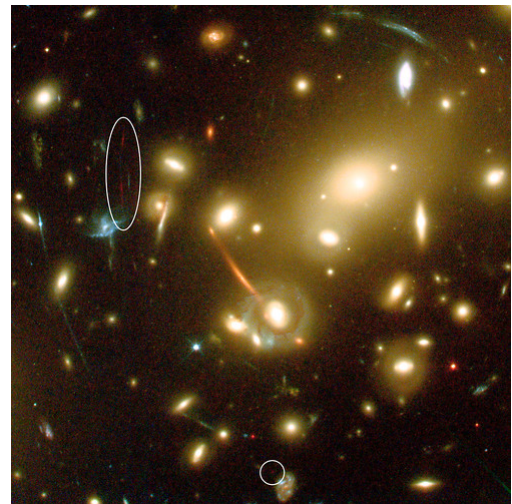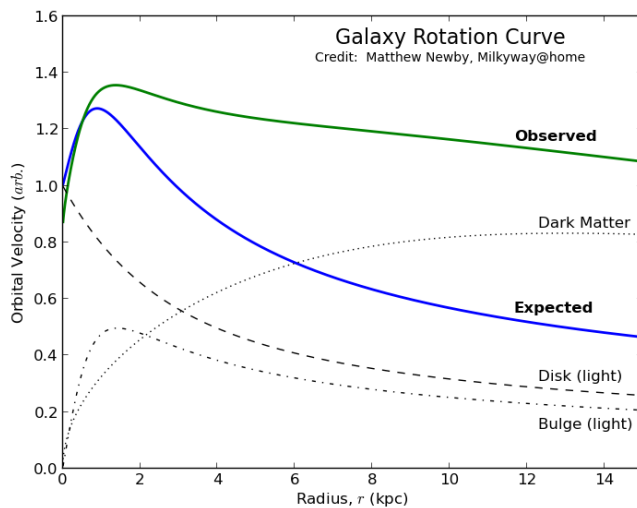
(a) Rotational Velocity curve of a galaxy, showing the expected and observed curves. Both the observed and expected curves include the Disk and Bulge, with the addition of the Dark Matter to the observed curve.
Source: M. Newby (Milkyway@home),
https://milkyway.cs.rpi.edu/milkyway/science.php#part2

(b) The Abell 2218 cluster which is lensing a structure behind it in the encircled area.
Source: ESA, NASA, J.-P. Kneib (Observatoire Midi-Pyrénées) and R. Ellis (Caltech),
https://asd.gsfc.nasa.gov/
blueshift/index.php/2012/12/18/
maggies-blog-farthest/

Figure 1.1: Clues for Dark Matter

A second hint can be found using gravitational lensing. When a massive object is between an observer and a background object, light from the latter is deflected or lensed (see Figure 1.1b). As this lensing phenomenon is dependent on the mass of the intervening object, this object can be 'weighed'.
When this is applied to clusters of galaxies, these clusters seem to be up to 400 times as massive as the light to mass ratio would indicate.

An argument of a more cosmological origin involves the Cosmic Microwave Background (CMB). Photons of this background were emitted about 300,000 years after the Big Bang in an era called recombination. There, the first neutral atoms crystalised out of the hot baryon-photon soup.
The Cosmic Microwave Background is highly isotropic. However, high-precision measurements by the Cosmic Background Explorer (COBE, 1992), Wilkinson Microwave Anisotropy Probe (WMAP, 2013) and Planck (2013) satellites uncovered anisotropies that hint at a 'dark' component within the matter density of the universe.
These anisotropies can be used to work out interactions and properties of the photons, matter, dark matter and dark energy content in the early universe.

1.2 Candidates

In order to be able to explain these effects, a dark matter candidate should have a very weak electromagnetic interaction. If this was not the case, such a candidate would have been visible in some part of the electromagnetic spectrum. Further more, it should allow for a vast amount of mass to be fairly evenly distributed over a galaxy's halo to allow for a smooth velocity curve.

Several propositions have been made for these properties. They can be roughly categorised into being either of astrophysical or particle nature.
Examples of proposed astrophysical objects are primordial black holes, MAssive Compact Halo Objects (MACHOs) and Milli-Second Pulsars (MSPs). However, there is a limit to the extent these objects might explain dark matter. Both lensing and the velocity curve might be explained by them, but the observation of baryon acoustic oscillations inhibits the amount of baryons needed to form such objects at the grand scale needed.

Instead, a particle nature seems more appropriate to explain the dark matter effects. One of the earliest theories of this kind expects the Standard Model's neutrino to fulfill the role of dark matter particle. However, upper limits on its mass show it to be too light to accomplish the gravitational effects needed. Moreover, a 'hot' dark matter type, having low-mass particles, would smoothen the largescale structure. The largescale structures are however rather clumpy.

Currently, the main candidate of a 'cold' dark matter is the Weakly Interactive Massive Particle (WIMP). Like the neutrino, it is non-baryonic, however it needs to be relatively heavy. Another property it should have is being stable on cosmological timescales. This requires it to have a (nearly-) conserved quantum number, which is commonly achieved by making the WIMP the lightest particle of a sector.

One such way is the introduction of supersymmetry. It introduces a supersymmetric version for each Standard Model (SM) particle, and its lightest particle (the LSP) would be a good candidate of a WIMP. The LSP might be able to annihilate with itself or decay, (indirectly) forming an SM particle which can then be observed. However, the crosssections and decayrates should be low to fulfill the stability for long timescales.

1.3 Particle Dark Matter in (Dwarf) Galaxies

If a WIMP can either decay or annihilate to SM particles, then this should be most apparent in locations with large mass densities. Locations of such high densities are the centers of galaxy halos, that is, at the center of galaxies.

The Galactic Centre (GC) would then seem to be a very good location for observations of these interactions. It is, however, a difficult case, as it has a highly complex background. To minimise effects of this, studies on the GC are done by filtering out its very center and considering a shell around it.

A location more accessible for observations are the dwarf galaxies around the Milky Way. These mini galaxies exhibit large mass-to-light ratios of up to $M/L \equiv \Upsilon \sim 1000$[1, 2] This makes them ideal candidates considering the signal-to-background ratio.

Another benefit of dwarf galaxies concerns the mass density profile associated with the dark matter. As there is debate over which profile to use, the smaller observable size gives an advantage over the Milky Way as a change in profile would give a massively different result for the GC, whereas this is less so in dwarfs.

They do pose challenges. The number of stars is very low compared to normal-sized galaxies, which affects the determination of some observables. The distance to these dwarfs ($d \sim 30\text{kpc}$) might pose another problem concerning the resolvability of stars. Both these aspects give rise to a low amount of tracer stars which are needed to correctly set up the model (See Section 5.1).

1.4 WIMPy Dark Matter annihilation

As dark matter is favoured to consist of WIMPs, annihilation of two such particles is expected to give rise to energetic SM particles. The involved interactions may give rise to γ-rays. These γ-rays are looked for by satellite based instruments such as Fermi-LAT. The γ-ray flux from locations such as a dwarf's core would then depend on two factors[3].

$$\frac{\mathrm{d}\phi_\gamma}{\mathrm{d}E_\gamma} = \phi_J^{PP}\left(E_\gamma\right) \times J\left(\Delta\Omega\right) \tag{1.1}$$

The factor ϕ_J^{PP} provides the particle physics properties of the dark matter, while the $J\left(\Delta\Omega\right)$ factor corresponds to its spatial distribution.

To be able to compare to other experiments, and possibly rule out or enhance the existence of a dark matter particle, Equation (1.1) is inverted to output the particle physics component from a measured γ-ray spectrum $\mathrm{d}\phi_\gamma/\mathrm{d}E_\gamma$ and estimated $J\left(\Delta\Omega\right)$. To this end, both the measurement of the spectrum and the calculation of this J-value and its uncertainty is important to interpreting the resulting limits on the character of the dark matter.

1.5 J-values

The factor $J(\Delta\Omega)$ introduced in Section 1.4 is dependent on the DM mass density, ρ_{DM}, integrated around a solid angle $\Delta\Omega = 2\pi\left[1 - \cos(\alpha_{int})\right]$ along the line of sight ($\mathrm{d}l$), with α_{int} the integration angle.

$$J = \iint\limits_{\Delta\Omega} \rho_{DM}^2(l,\Omega)\,\mathrm{d}\Omega\,\mathrm{d}l \tag{1.2}$$

In the case of dark matter decay, we use the D-value instead of J, with D the integral of ρ_{DM} rather than its square.

Eventhough Equation 1.2 seems to be simple, it poses a problem to compute. The dark matter mass density ρ_{DM} is the integral component of the J-value, however, the density cannot be measured directly. To this end, techniques (such as Dynamical Mass Modelling) have been developed to infer this density. A requirement for Dynamical Mass Modelling, commonly called Jeans Analysis, is having spectroscopic measurements of stars in the dwarf galaxy to infer rotational velocities.

1.5.1 Estimation

Circumventing the extensive calculation of (1.2) and the required mass density ρ_{DM}, a scaling relationship was found between the heliocentric distance d and J. [3] In Figure 1.2, this relationship is shown, together with J-values as calculated by various groups.

Fitted to J-values calculated by Geringer-Sameth, Koushiappas, and Walker [4], the relationship takes the following form,

$$\log_{10}\left(\frac{J_{pred}}{J_0}\right) = -2\log_{10}\left(\frac{d}{D_0}\right), \tag{1.3}$$

with $J_0 = 18.1$ GeV^2/cm^{-5} and $D_0 = 100$kpc.
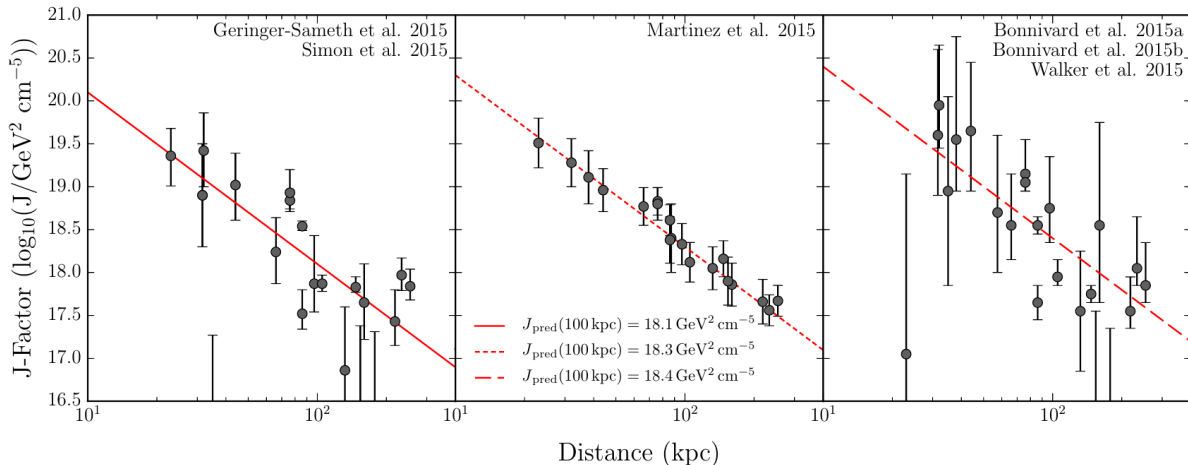
Figure 5. Relationship between the distances and spectroscopically determined J-factors of known dSphs is derived with three different techniques: (*left*) non-informative priors (Geringer-Sameth et al. 2015a), (*center*) Bayesian hierarchical modeling (Martinez 2015), and (*right*) allowing for more flexible parametrizations of the stellar distribution and orbital anisotropy profile (Bonnivard et al. 2015a). We also include recently derived J-factor estimates for Reticulum II (Simon et al. 2015; Bonnivard et al. 2015b) and Tucana II (Walker et al. 2015b) with J-factors for other dSphs that were calculated in a similar manner (see references for each panel). We fit the J-factor scaling relation (Equation 2) to the data in each panel, yielding $\log_{10}(J_0/\,\mathrm{GeV^2\,cm^{-5}}) = \{18.1, 18.3, 18.4\}$, for the left, center, and right panels, respectively; these relationships are plotted as solid, short dashed, and long dashed red lines.

Figure 1.2: From [3]. Comparing the scaling relationship (1.3) to data from various groups. The average measurement uncertainty is bigger than the intrinsic scatter relative to the scaling.

For some newly discovered dwarf galaxies, the required spectroscopic measurements for the Jeans analysis, are not yet available. As (1.3) gives an estimate for these objects, they can still be used in analyses of the particle physics factor ϕ_J^{PP}.

The use of Equation 1.3 is justified by assuming these new dwarfs inhabit similar dark matter haloes as the currently known dwarfs do. This holds to a certain extent, as there are now at least 3 classes of dwarf galaxy identified (see Section 5.1). Most of these dwarf galaxies are dwarf spheroidal (dSph) galaxies.

In addition, the average measurement uncertainty on the calculated J-values is bigger than their scattering relative to the scaling itself.

1.5.2 Jeans Analysis and J-value Calculation

In this thesis, the setup to calculate the J-value utilising Jeans analysis is explored. With the aforementioned Jeans analysis (see Section 2), a dark matter mass density ρ_{DM} can be inferred. It may be obtained by constructing a galaxy's halo from measurements on this halo's stars, as these are the 'microscopic' tracers available to us.

In an ideal case, the full velocity and position vectors of a tracer star is known. However, only the line of sight component of the velocity can be measured (by taking spectroscopic measurements). Similarly, the position vector cannot be fully measured as the distance cannot be resolved.

This is where the Jeans analysis comes in. In essence, it employs averaged quantities provided by a phasespace argument, helping to deal with the missing components to the velocity and position.
Using it, an equation can be derived to obtain radial velocities from an underlying model involving the mass density function. By comparing the calculated velocities with measured radial velocity of tracer stars, the model can be updated thus fitting the mass density function.

The derivation of the equation set forth by the Jeans analysis requires the introduction of other quantities such as velocity anisotropy and stellar density. In Section 3, these are listed and some commonly used parametric forms are given. They might be linked to other observables such as surface brightness to better follow the properties of the reconstructed halo.

As the derived equations are a combination of both derivatives and integrals, fitting the mass density function is hard to do analytically. Because of the number of parameters introduced for the parametric models, this is accomplished using numerical methods (see Section 4).

Finally, some extra considerations are mentioned in Section 5 to further constrain the calculation of the models and thus the J-value.

2. Deriving the Jeans Equation

To find the dark matter mass density of a galaxy it is helpful to look at the system in a 6D phasespace (position and momentum of the stars). On this phasespace a continuity equation (2.1) can be formulated. With some algebraic manipulations this continuity equation can then be identified as the Collisionless Boltzmann Equation (2.3).

By further manipulation of the Collisionless Boltzmann Equation, a new equation is derived called the Jeans equation (2.10). This final equation helps in coping with the missing components to the position and velocity vectors by introducing averaged quantities of them. In this chapter the derivation of this equation is worked out.
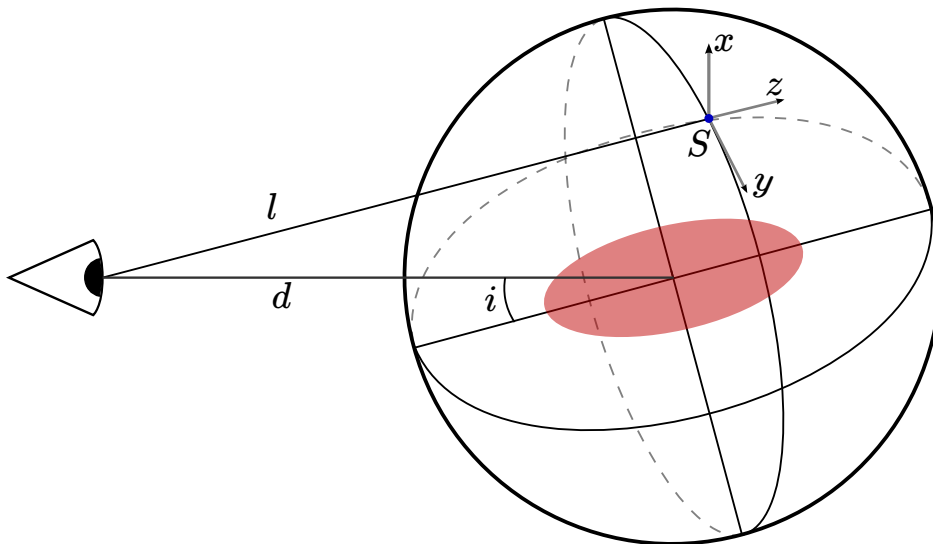
Figure 2.1: Coordinate system for a star S within a dwarf galaxy (shaded area) and its line of sight l. Velocities cannot be detected along the x and y axis, while their position might be resolved. Conversely, along the line of sight z, velocities can be mapped using doppler shift but position is non-resolvable.

2.1 Collisionless Boltzmann Equation

Setting up a 6D phasespace is helpful to be able to handle the positions and velocities which cannot be measured directly (see Figure 2.1). In this phasespace, stars are the points which can be followed throughout it.

Define the coordinates of this phasespace as $\vec{w} = (\vec{x}, \vec{u})$ with $\vec{x}$ and $\vec{u}$ the (cartesian) distance and velocity. The combined gravity from the stars and the dark matter gives rise to a smooth potential $\Phi(\vec{x}, t)$[1]. Given $\dot{\vec{u}} = -\nabla\Phi$, we have $\dot{\vec{w}} = (\dot{\vec{x}}, \dot{\vec{u}}) = (\vec{u}, -\nabla\Phi)$. In this phasespace a distribution function $f(\vec{w}, t)$ gives the

---

[1]Note that the mass of the stars is assumed to be negligible

amount of stars per phasespace volume $d^6w = d^3x d^3u$. Since there cannot be a negative amount of stars, a constraint is introduced as $f \geq 0$.

As stars do not suddenly jump from one phasespace coordinate to another but rather drift smoothly, a continuity equation can be formulated

$$\frac{\partial f}{\partial t} + \sum_{\alpha=1}^{6} \frac{\partial (f \dot{w}_\alpha)}{\partial w_\alpha} = 0. \tag{2.1}$$

The derivatives in the sum can be simplified using

$$\sum_{\alpha=1}^{6} \frac{\partial \dot{w}_\alpha}{\partial w_\alpha} = \sum_{i=1}^{3} \left(\frac{\partial u_i}{\partial x_i} + \frac{\partial \dot{u}_i}{\partial u_i} \right) = \sum_{i=1}^{3} -\frac{\partial}{\partial u_i} \left(\frac{\partial \Phi}{\partial x_i} \right) = 0. \tag{2.2}$$

Here u_i does not depend on x_i explicitly, just as $\dot{u}_i = -\partial \Phi(\vec{x})/\partial x_i$ [2] does not depend on u_i.

Now (2.1) can be rewritten to the Collisionless Boltzmann Equation

$$\frac{\partial f}{\partial t} + \sum_{\alpha=1}^{6} \dot{w}_\alpha \frac{\partial f}{\partial w_\alpha} = 0 \tag{2.3a}$$

$$= \frac{\partial f}{\partial t} + \sum_{i=1}^{3} \left(u_i \frac{\partial f}{\partial x_i} - \frac{\partial \Phi}{\partial x_i} \frac{\partial f}{\partial u_i} \right) = \frac{\mathrm{d}f}{\mathrm{d}t} \tag{2.3b}$$

$$= \frac{\partial f}{\partial t} + \vec{u} \cdot \vec{\nabla}_x f - \vec{\nabla}\Phi \cdot \vec{\nabla}_u f. \tag{2.3c}$$

In (2.3b) the Liouville equation (A.1.1) of f can be recognised. (2.3c) gives more feel for what is stated.

A nice thing about the distribution function is that it can be applied to various populations separately. This way we can for example define

$$f_{tot} = f_{DM} + f_{stars}. \tag{2.4}$$

2.2   Deriving the Jeans equation

The derivation of the Jeans equation is accomplished by integrating the Collisionless Boltzmann Equation over all velocities in the 6D phasespace.

The first part is concerned with finding the first and second moment of the Collisionless Boltzmann Equation. The first moment is found by directly integrating (2.3) over the velocities. The second moment, however, needs the Collisionless Boltzmann Equation to be multiplied with one of the velocities u_i before doing the integration.

In the second part, these moments are combined into one expression, the Jeans equation (2.10).

The introduction of a shorthand for a quantity Q, averaged over all velocities, as

$$\langle Q \rangle = \frac{\int Q f \, \mathrm{d}^3 u}{\int f \, \mathrm{d}^3 u} \quad = \frac{1}{\nu} \int Q f \, \mathrm{d}^3 u \tag{2.5}$$

simplifies the resulting expressions.

Here,

$$\nu = \int f \, \mathrm{d}^3 u \tag{2.6}$$

is the integrated phasespace density as used to set up the phasespace.

---

[2] In reality $\dot{\vec{u}}$ differs from $-\nabla\Phi$ due to individual encounters

2.2.1   Part I: First Moment

Something alike (2.5) can be achieved with the Collisionless Boltzmann Equation. Integrating (2.3b) over all velocities we get

$$\int \frac{\mathrm{d}f}{\mathrm{d}t}\,\mathrm{d}^3u = \int \frac{\partial f}{\partial t}\,\mathrm{d}^3u + \sum_{i=1}^{3}\left(\int u_i\frac{\partial f}{\partial x_i}\,\mathrm{d}^3u - \int \frac{\partial \Phi}{\partial x_i}\frac{\partial f}{\partial u_i}\,\mathrm{d}^3u\right) = 0.$$

The integrals and derivatives can be swapped because time, space and velocity are independent quantities.

$$= \frac{\partial}{\partial t}\int f\,\mathrm{d}^3u + \sum_{i=1}^{3}\left(\frac{\partial}{\partial x_i}\int u_i f\,\mathrm{d}^3u - \frac{\partial \Phi}{\partial x_i}\int \frac{\partial f}{\partial u_i}\,\mathrm{d}^3u\right)$$

Rewritten in terms of averages (see (2.5)), introducing $\langle u_i\rangle$, and the density ν, we find

$$= \frac{\partial \nu}{\partial t} + \sum_{i=1}^{3}\left(\frac{\partial}{\partial x_i}\nu\langle u_i\rangle - \frac{\partial \Phi}{\partial x_i}\int \frac{\partial f}{\partial u_i}\,\mathrm{d}^3u\right).$$

As there are no phasespace objects with infinite velocities, the integral in the right-most term equals zero. This can be shown by rewriting the integral to

$$\int \frac{\partial f}{\partial u_i}\,\mathrm{d}^3u = \iiint \frac{\partial f}{\partial u_i}\,\mathrm{d}u_i\,\mathrm{d}u_j\,\mathrm{d}u_k$$

$$= \iint \mathrm{d}u_j\,\mathrm{d}u_k \int \mathrm{d}f$$

$$= \iint \mathrm{d}u_j\,\mathrm{d}u_k f$$

$$= 0. \tag{2.7}$$

Thus we obtain the first moment of the Collisionless Boltzmann Equation, a 3-D continuity equation, as

$$\int \frac{\mathrm{d}f}{\mathrm{d}t}\,\mathrm{d}^3u = \frac{\partial \nu}{\partial t} + \sum_{i=1}^{3}\frac{\partial\left(\nu\langle u_i\rangle\right)}{\partial x_i} = 0 = \frac{\partial \nu}{\partial t} + \vec{\nabla}_x \cdot \nu\langle\vec{u}\rangle. \tag{2.8}$$

2.2.2   Part II: Second Moment

By first multiplying (2.3b) with one of the velocities u_j, and then integrating over the velocities, the second moment of the Collisionless Boltzmann Equation is obtained.

$$\int u_j\frac{\mathrm{d}f}{\mathrm{d}t}\,\mathrm{d}^3u = \int u_j\frac{\partial f}{\partial t}\,\mathrm{d}^3u + \sum_{i=1}^{3}\left(\int u_j u_i\frac{\partial f}{\partial x_i}\,\mathrm{d}^3u - \int u_j\frac{\partial \Phi}{\partial x_i}\frac{\partial f}{\partial u_i}\,\mathrm{d}^3u\right) = 0 \tag{2.9a}$$

The integrals and derivatives can again be swapped.

$$= \frac{\partial}{\partial t}\int u_j f\,\mathrm{d}^3u + \sum_{i=1}^{3}\left(\frac{\partial}{\partial x_i}\int u_j u_i f\,\mathrm{d}^3u - \frac{\partial \Phi}{\partial x_i}\int u_j\frac{\partial f}{\partial u_i}\,\mathrm{d}^3u\right) \tag{2.9b}$$

$$= \frac{\partial\left(\nu\langle u_j\rangle\right)}{\partial t} + \sum_{i=1}^{3}\left(\frac{\partial}{\partial x_i}\nu\langle u_j u_i\rangle - \frac{\partial \Phi}{\partial x_i}\int u_j\frac{\partial f}{\partial u_i}\,\mathrm{d}^3u\right) \tag{2.9c}$$

The right integral is zero for $j \neq i$ and gives $-\nu$ for $j = i$ (see below).

$$= \frac{\partial\left(\nu\langle u_j\rangle\right)}{\partial t} + \sum_{i=1}^{3}\frac{\partial\left(\nu\langle u_j u_i\rangle\right)}{\partial x_i} + \nu\frac{\partial \Phi}{\partial x_j} = 0 \tag{2.9d}$$

This equation is different from (2.8) by having a derivative of the potential, Φ, the time derivative of $\nu\langle u_j\rangle$ instead of ν and the position derivative of $\nu\langle u_j u_i\rangle$ instead of $\nu\langle u_i\rangle$.

In (2.9c), the right integral was set to $-\nu$ when the coordinates i and j are the same or to zero when they are different. This can be shown by partially integrating this integral.

$$\int u_j \frac{\partial f}{\partial u_i}\, \mathrm{d}^3 u = \int \frac{\partial\, (u_j f)}{\partial u_i}\, \mathrm{d}^3 u - \int f \frac{\partial u_j}{\partial u_i}\, \mathrm{d}^4 u = -\nu \langle \frac{\partial u_j}{\partial u_i}\rangle$$

In this expression the first term can be set to zero due to the infinite velocities argument (2.7).
If $i \neq j$, the second integral follows the same logic and returns zero. However, when $i = j$, this integral is the regular phasespace integral (2.6) thus returning ν.

2.2.3 The Jeans equation

To obtain the Jeans equation, the previous two equations are combined into one expression by multiplying (2.8) with $\langle u_j \rangle$ and subtracting this from (2.9d).

$$\frac{\partial\, (\nu \langle u_j \rangle)}{\partial t} + \sum_{i=1}^{3} \frac{\partial\, (\nu \langle u_j u_i \rangle)}{\partial x_i} + \nu \frac{\partial \Phi}{\partial x_j} - \left(\langle u_j \rangle \frac{\partial \nu}{\partial t} + \langle u_j \rangle \sum_{i=1}^{3} \frac{\partial\, (\nu \langle u_i \rangle)}{\partial x_i} \right) = 0$$

$$= \nu \frac{\partial \langle u_j \rangle}{\partial t} + \nu \frac{\partial \Phi}{\partial x_j} + \sum_{i=1}^{3} \left(\frac{\partial\, (\nu \langle u_j u_i \rangle)}{\partial x_i} - \langle u_j \rangle \frac{\partial\, (\nu \langle u_i \rangle)}{\partial x_i} \right)$$

$$= \nu \frac{\partial \langle u_j \rangle}{\partial t} + \nu \frac{\partial \Phi}{\partial x_j} + \sum_{i=1}^{3} \left\{ \frac{\partial\, (\nu\, [\langle u_j u_i \rangle - \langle u_j \rangle \langle u_i \rangle])}{\partial x_i} + \nu \left(\frac{\partial \langle u_j u_i \rangle}{\partial x_i} - \langle u_j \rangle \frac{\partial \langle u_i \rangle}{\partial x_i} \right) \right\}$$

Defining the stress tensor $\sigma_{ij}^2 = \langle (u_i - \langle u_i \rangle)(u_j - \langle u_j \rangle) \rangle = \langle u_i u_j \rangle - \langle u_i \rangle \langle u_j \rangle$, we get

$$= \nu \frac{\partial \langle u_j \rangle}{\partial t} + \nu \frac{\partial \Phi}{\partial x_j} + \sum_{i=1}^{3} \left\{ \frac{\partial\, (\nu \sigma_{ij}^2)}{\partial x_i} + \nu \langle u_i \rangle \frac{\partial \langle u_j \rangle}{\partial x_i} \right\} = 0.$$

By interpreting $\nu \sigma_{ij}^2$ as pressure and ν as density, this equation can be seen as a scalar form of Euler's equation (A.2.1).

$$\nu \frac{\partial \langle u_j \rangle}{\partial t} + \sum_{i=1}^{3} \nu \langle u_i \rangle \frac{\partial \langle u_j \rangle}{\partial x_i} = -\nu \frac{\partial \Phi}{\partial x_j} - \sum_{i=1}^{3} \frac{\partial\, (\nu \sigma_{ij}^2)}{\partial x_i} \qquad (2.10)$$

Equation (2.10) has no explicit velocity component. Instead, these have been replaced by averages of the velocity. Similarly, the problem posed by not being able to resolve the radial position is lifted as the explicit position components have vanished.

2.2.4 The Jeans equation in different coordinates

The Jeans equation is mostly applied to star clusters and galaxies. These are generally non-cartesian systems. To get the Jeans equation in a different coordinate system, the Collisionless Boltzmann Equation (2.3) needs to be rewritten to this coordinate system before taking the first and second moments.
In cartesian coordinates we have $\langle u_i \rangle$ with i cycling through (x, y, z). In a different coordinate system, the various $\langle u_i \rangle$ moments can have different behaviors. So, instead of (implicitly) getting one equation as in Section 2.2.2, there will be three, i.e. (r, θ, z).
In Appendix A.4 cylindrical and spherical versions of the Collisionless Boltzmann and Jeans equations can be found.

2.3 Working with the spherical radial Jeans equation

In Section 2.2, the derivation of the Jeans equation(s) is shown. Because the dwarf galaxies are in first order approximation spherical objects, the Jeans equations in spherical coordinates are the relevant set.
Of interest is then the spherical radial Jeans equation (A.4.8).This equation is in a general form, and can be simplified with appropriate assumptions.

The first assumption is steady state ($\frac{\partial}{\partial t} = 0$), effectively erasing the left most term of (2.10). Dynamical timescales for a dwarf galaxy are so long that no time-dependence of quantities can be taken into account.

Most systems can be further constrained by hydrodynamical equilibrium. When a system is in hydrodynamical equilibrium, the forces are roughly balanced. This implies that there is no net radial motion ($\langle u_r \rangle = 0$). With the average radial velocity being zero, some elements of the stress tensor σ_{ij}^2 can be rewritten to

$$\sigma_{r\alpha}^2 = \langle u_r u_\alpha \rangle - \langle u_r \rangle \langle u_\alpha \rangle = \langle u_r u_\alpha \rangle, \tag{2.11}$$

where α is one of the coordinates (r, θ, φ).
Further simplification is achieved by requiring spherical symmetry, setting

$$\langle u_\theta \rangle = \langle u_\varphi \rangle = 0, \quad \sigma_{r\theta}^2 = \sigma_{r\varphi}^2 = \sigma_{\theta\varphi}^2 = 0, \quad \sigma_{\theta\theta}^2 = \sigma_{\varphi\varphi}^2 := \sigma_\varphi^2. \tag{2.12}$$

With the above sets of equations, we can rewrite two terms. The first term uses $\langle u_r^2 \rangle = \sigma_{rr}^2 := \sigma_r^2$.
Secondly, the $\left(\langle u_r^2 \rangle - \langle u_\varphi^2 \rangle \right)$ term in the Jeans equation can be recast in terms of the anisotropy parameter β_{ani} and the radial velocity dispersion σ_r^2, where

$$\beta_{ani} = 1 - \frac{\langle u_\varphi^2 \rangle}{\langle u_r^2 \rangle} = 1 - \frac{\sigma_\varphi^2}{\sigma_r^2}. \tag{2.13}$$

The anisotropy parameter β_{ani} can take values from $-\infty$ up to 1, where the first value corresponds to circular and the second value to radial isotropy. There is full isotropy when $\beta_{ani} = 0$.

With these changes, the spherical radial Jeans equation becomes

$$\frac{1}{\nu} \frac{\partial \left(\nu \sigma_r^2 \right)}{\partial r} + 2\beta_{ani} \frac{\sigma_r^2}{r} = \frac{\partial \Phi}{\partial r} = -\frac{GM(r)}{r^2}, \tag{2.14}$$

relating the total enclosed mass $M(r)$ to the radial dynamical pressure $P = \nu \sigma_r^2$.

2.3.1 Solution to the spherical radial Jeans equation

The radial Jeans equation (2.14) is now the tool to analyse the various dwarf galaxies.
A general solution to this equation can be set up as

$$\nu(r)\sigma_r^2(r) = \frac{1}{f(r)} \int_r^\infty f(s)\nu(s)\frac{GM(s)}{s^2} \, \mathrm{d}s, \tag{2.15}$$

with

$$f(r) = f_{r_1} \exp \left(\int_{r_1}^r \frac{2}{s} \beta_{ani}(s) \, \mathrm{d}s \right), \tag{2.16}$$

where the terms of interest are the $\nu(r)\sigma_r^2(r)$ and $M(r)$ terms. The $M(r)$ term contains the dark matter mass distribution ρ_{DM} which is needed to perform the integral of (1.2). The $\nu(r)\sigma_r^2(r)$ term contains the radial dispersion which is the observationally accessible quantity in our context.

The main obstacle posed by (2.14) (and its solution (2.15)) is a degeneracy between the mass $M(r)$ and the anisotropy $\beta_{ani}(r)$, known as the Mass-Anisotropy-Degeneracy (MAD).

By assuming appropriate values to $\beta_{ani}(r)$, it is possible to lift the MAD and get analytic expressions for the mass profile. A rewritten form of (2.14) makes this easier to discern,

$$u_{circ}^2 = \frac{GM(r)}{r} = -\sigma_r^2 \left(\frac{\mathrm{d}\ln\nu}{\mathrm{d}\ln r} + \frac{\mathrm{d}\ln\sigma_r^2}{\mathrm{d}\ln r} + 2\beta_{ani}(r) \right). \tag{2.17}$$

Instead of relying on a specific value for $\beta_{ani}(r)$ to lift the degeneracy and calculate the enclosed mass $M(r)$, we will be choosing parametric models for the anisotropy and mass (see Section 3). Specifically, we will be using a mass density $\rho(s)$ such that

$$M(r) = 4\pi \int_0^r \rho(s)s^2 \,\mathrm{d}s.$$

Note that the mass contribution of stars is assumed to be negligible. This results in a halo dominated by the dark matter. Therefore, $\rho(r)$ can be replaced by $\rho_{DM}(r)$.

As the internal velocities of the stars cannot be resolved, quantities like ν and σ_r^2 have to be projected along the line of sight (see Figure 2.1). This projecting can be done using Abel transforms (A.3.1a, A.3.1b). With the Abel transforms, the general solution can then be written as

$$I(r)\sigma_p^2(r) = 2 \int_r^\infty \left(1 - \beta_{ani}(s)\frac{r^2}{s^2} \right) \nu(s)\sigma_r^2(s)\frac{s}{\sqrt{s^2 - r^2}} \,\mathrm{d}s, \tag{2.18}$$

with

$$I(r) = \int_r^\infty \frac{\nu(s)s}{\sqrt{s^2 - r^2}} \,\mathrm{d}s. \tag{2.19}$$

With σ_p the projected velocity dispersion, $I(R)$ the projected stellar density and β_{ani} the velocity dispersion anisotropy. While the first one is directly observable using Doppler shifts, the others are not. To overcome this, $I(R)$ and $\beta_{ani}(r)$ are assumed to follow profiles as outlined in the next Section.

3. Inputs to the Jeans equations

The derivation of (2.18) introduced quantities like the velocity anisotropy $\beta_{ani}(r)$, stellar density $\nu(r)$ and mass density ρ_{DM}, these have to be linked to observables to model the dwarf galaxy correctly.
Such observables include the total luminosity L of the galaxy, the line-of-sight velocities u_{los} and positions of individual stars, the total velocity dispersion σ_{tot} and the radius from the center of the galaxy at which the light intensity is halved, called the half-light radius $r_{1/2}$.

To link these observables and the introduced quantities, profiles can be used. The profile parameterises its quantity in the form of exponents and scaling which have to be fitted later. In this Section, some profiles are explored for the mass density ρ_{DM}, velocity dispersion anisotropy $\beta_{ani}(r)$ and the stellar density $\nu(r)$ or projected stellar density $I(r)$.

Some of these observables can be used to set limits or fit the above mentioned profiles directly. For example, there is a relationship between the mass at the 3D half-light radius and the total velocity dispersion assuming the enclosed mass is constrained only at the half-light radius by the Jeans equation [5, 6].

$$M\left(r_{1/2}\right) = 3\sigma_{tot}^2/G. \tag{3.1}$$

3.1 Mass density profiles

Throughout the literature, many profiles have been suggested for ρ_{DM}. One of the first profiles proposed was the Navarro, Frenk and White (NFW) profile.[7] It was based on large scale N-body simulations of collisionless dark matter. Later phenomologically-oriented profiles such as the Burkert (3.2)[8] and Moore profiles (see Table 3.1)[9] have been introduced as they have different behaviours at small radii (being cored or cuspy) and/or large radii (falling off faster or slower).

$$\rho_{\text{Burkert}} = \frac{\rho_{\text{s}}}{(1 + r/r_{\text{s}})\left(1 + (r/r_{\text{s}})^2\right)} = \frac{\rho_0 r_s^3}{(r_s + r)\left(r_s^2 + r^2\right)} \tag{3.2}$$

Here we will be reviewing the Einasto ρ_{DM}^{Ein} [10, 11] and the Zhao-Hernquist ρ_{DM}^{Zhao} [12] mass density profiles as these are currently the most favored profiles [13, 14].

The Einasto profile (3.3) is a cored profile. This means that at small radii, the profile will converge to a finite value. This can be contrasted to a cuspy profile which diverges at small radii.
The profile can be defined as

$$\rho_{DM}^{Ein}(r) = \rho_{-2} \exp\left(-\frac{2}{\alpha_{Ein}}\left[\left(\frac{r}{r_{-2}}\right)^{\alpha_{Ein}} - 1\right]\right), \tag{3.3}$$

where ρ_{-2} and r_{-2} are characteristic values at $\rho(r) \propto r^{-2}$[15].
The parameter $\alpha_{Ein} > 0$ is the logarithmic slope, controlling the fall off with increasing radius. Note that due to the nature of this parameter, the profile always retains a core.
The values of the scaling radius r_{-2} and the scaling mass density ρ_{-2} are intrinsic to each dwarf galaxy and have to be found for each dwarf galaxy individually.

Table 3.1: Parameters to the Zhao-Hernquist profile family (3.4) retrieving common profiles. The upper part are common mass densities, while the lower are the stellar densities.

	α	β	γ
NFW	1	3	1
sNFW	1	3.5	1
Moore	1.5	3	1.5
Isothermal	2	2	0
Plummer	2	5	0

The Zhao-Hernquist profile (3.4) describes a family of often used profiles such as the NFW profile and allows our fitting mechanism to select the most appropriate of these profiles (See Table 3.1).

$$\rho_{DM}^{Zhao}(r) = \rho_s \left(\frac{r}{r_s} \right)^{-\gamma} \left[1 + \left(\frac{r}{r_s} \right)^{\alpha} \right]^{\frac{\gamma - \beta}{\alpha}} \tag{3.4}$$

with

$$\left. \frac{\mathrm{d} \log \rho}{\mathrm{d} \log r} \right|_{r \ll r_s} = -\gamma \quad \text{and} \quad \left. \frac{\mathrm{d} \log \rho}{\mathrm{d} \log r} \right|_{r \gg r_s} = -\beta$$

and α reflecting the sharpness of the transition at $r = r_s$ [12].
Note that just as r_{-2} in (3.4), r_s is just a scaling radius, to be determined for each dwarf galaxy separately. With the above definition, we can find ρ_s with $\rho_s = \rho(r_s) \cdot 2^{\frac{\beta - \gamma}{\alpha}}$.

To compare the Zhao profile with the Einasto profile, the scaling radius r_s can be rewritten to an equivalent of r_{-2} with

$$r_{-2}^{Zhao} = r_s \times \left(\frac{\beta - 2}{2 - \gamma} \right)^{-1/\alpha} \tag{3.5}$$
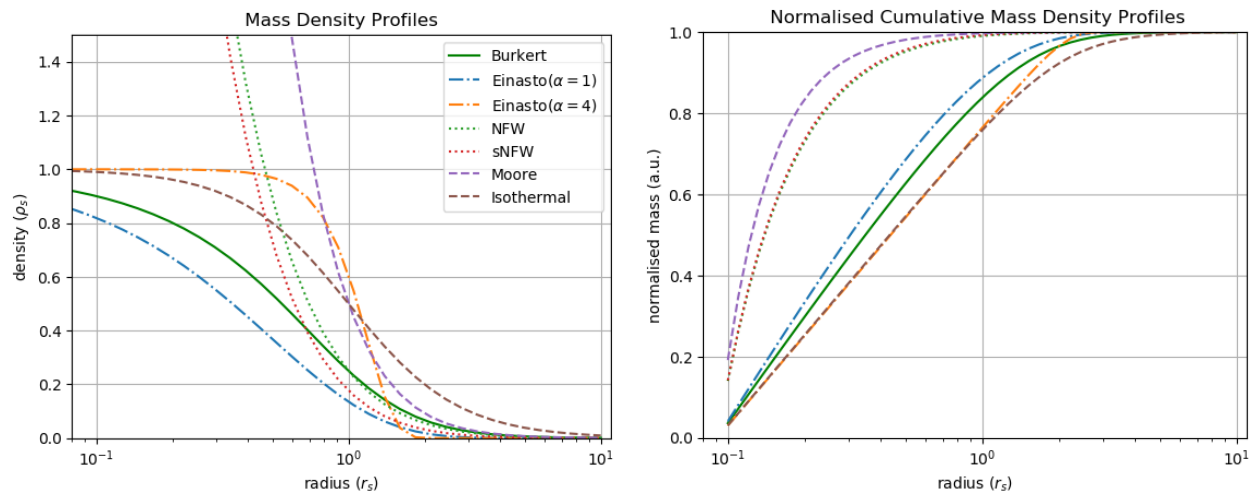
(a) The Einasto and Zhao families of mass density profiles plotted.

(b) The corresponding integrated and normalized mass profiles.

Figure 3.1: The Zhao family with $\gamma \geq 1$ is easily identified as they explode at small radii. For illustration purposes, the Burkert profile (3.2) is mentioned as it shows properties of the other two profiles. It obtains a flat central density while at the same time exhibiting a fall off common to the NFW profile at larger radii.

The main difference between the Einasto profile and the Zhao-Hernquist family is the ability to retrieve "cuspy" or "cored" profiles. As can be seen in Figure 3.1, the Einasto profiles are finite at $r = 0$. This is the reason it is called a cored profile.

The Zhao-Hernquist profile is able to retrieve a cored profile with $\gamma = 0$ (e.g. the Isothermal profile), while attaining a cuspy profile with $\gamma \geq 0$ (e.g. NFW profile).

Whether the cuspy or the cored profiles are preferred is ongoing debate. As mentioned earlier, high resolution N-body simulations favour the NFW profile, corresponding to a cuspy profile. However, Agnello and Evans [16] show that a NFW profile is disqualified as a viable profile for at least the Sculptor dSph using virial methods. One of the attributed causes is the unknown substructure of DM haloes.

In fact, there is a tendency to flatter profiles for DM dominated dwarf galaxies, while the cuspy profiles are more in accordance to the larger galaxies and clusters thereof [17].

In Del Popolo et al. [18] a possible mechanism to flatten initially cuspy profiles is explored. They simulate the evolution of dwarfs incorporating the baryonic evolution. In the less massive galaxies, the center potential well is not deep enough to preserve a cusp as the dark matter is heated due to the dynamical friction caused by the baryonic component. Meanwhile, in massive galaxies and clusters of galaxies, the potential is deep enough to preserve the cusp, effectively keeping the DM cold, thus explaining the suggestion of the NFW profile for such objects.

According to Bonnivard et al. [14], the difference between the cored Zhao and Einasto profiles are small. Even in *maximum knowledge* situations, in which mock data has been generated with a certain profile for *The Gaia Challenge*[1], they find that the profiles match to a high degree.

Likewise, An and Zhao [19] concluded that the Einasto and Zhao profiles are qualitatively equal for the cored profiles, after doing a full analysis on the generalised Einasto and Zhao profiles.

Because of this, and because of its better computability, they recommend to use the Einasto profile.

3.2   Light profiles

In the projected solution of the Jeans equation (2.18) there are two terms that can be related to a light profile (the surface brightness $I(R)$ and the stellar density ν). Due to (2.19), either of them is needed. The other can be computed, either analytically or numerically, by applying the relevant Abel transform (A.3.1).

The surface brightness is more readily compared to observational data. This happens because the total luminosity is the integral of the surface brightness over the extent of the galaxy. Because of this, we will be reviewing (mostly) the surface brightness profiles instead of their related stellar densities. Note that in the literature, the symbols Σ and I are used interchangingly for the same surface brightness.

Conversely, if the positioning of stars can be resolved, the stellar density can be fitted to these positions, resulting in a more appropriate choice of profile (and parameters).

Traditional parametrisations of the light profile are the Plummer (3.6), King (3.7), Sérsic (3.8) and exponential (3.9) profiles [14]. Of these, the Plummer profile is used the most. Since its inception, this profile has been applied to globular clusters [20]. Because of the analytical properties it is a favorite toy-model for simulations despite the too large fall off at large distances.

The later profiles have been proposed to better fit certain aspects of globular clusters with the exponential suggested for dwarf spheroidal galaxies specifically.

---

[1] http://astrowiki.ph.surrey.ac.uk/dokuwiki/doku.php

$$I^{Plummer}(R) = \frac{L}{\pi r_{1/2}} \frac{1}{\left[1 + \left(\frac{R}{r_{1/2}}\right)^2\right]^2} \tag{3.6}$$

$$I^{King}(R) = I_0 \left(\left[1 + \left(\frac{R}{r_c}\right)^2\right]^{-1/2} - \left[1 + \left(\frac{r_{lim}}{r_c}\right)^2\right]^{-1/2}\right)^2 \tag{3.7}$$

$$I^{Sersic}(R) = I_0 \exp\left(-b_n \left[\left(\frac{R}{r_c}\right)^{1/n} - 1\right]\right) \tag{3.8}$$

$$I^{exp}(R) = I_0 \exp\left(-\frac{R}{r_c}\right) \tag{3.9}$$

where for all profiles I_0 is a normalization and $r_{1/2}$, r_c and r_{lim} are respectively the half-light radius, core radius, and the maximum extent after which the density goes to zero. Furthermore, parameters to the Sérsic profile are $b_n = 2n - 1/3 + 0.009876/n$ and $n \gtrsim 0.5$ a number to control the logarithmic fall off.

In their analysis, [14] finds that the King and Sérsic both undershoot the light profile at large radii, while simultaneously over estimating it at small radii.
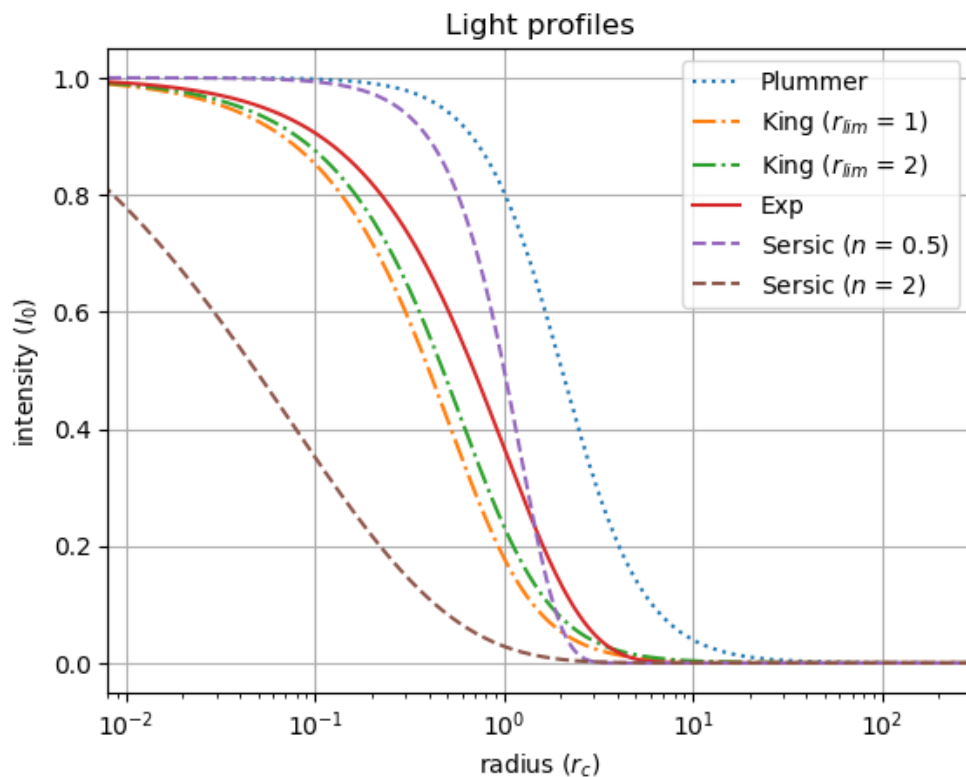
Figure 3.2: The various light profiles in a log plot

A more flexible profile is obtained by utilizing the Zhao-Hernquist family (3.4) to also parametrise the stellar density $\nu(r)$. Then, after projecting, it can be compared to the total luminosity.

In fact, the 3D stellar density formulation of the Plummer profile is part of the Zhao-Hernquist family with $(\alpha, \beta, \gamma) = (2, 5, 0)$ and normalisation $\nu_0 = \frac{3L}{4\pi r_{1/2}^3}$ (See Table 3.1).

Because of the flexibility of this profile family, [14] recommends to use the Zhao-Hernquist family or the Plummer profile specifically for the light profile.
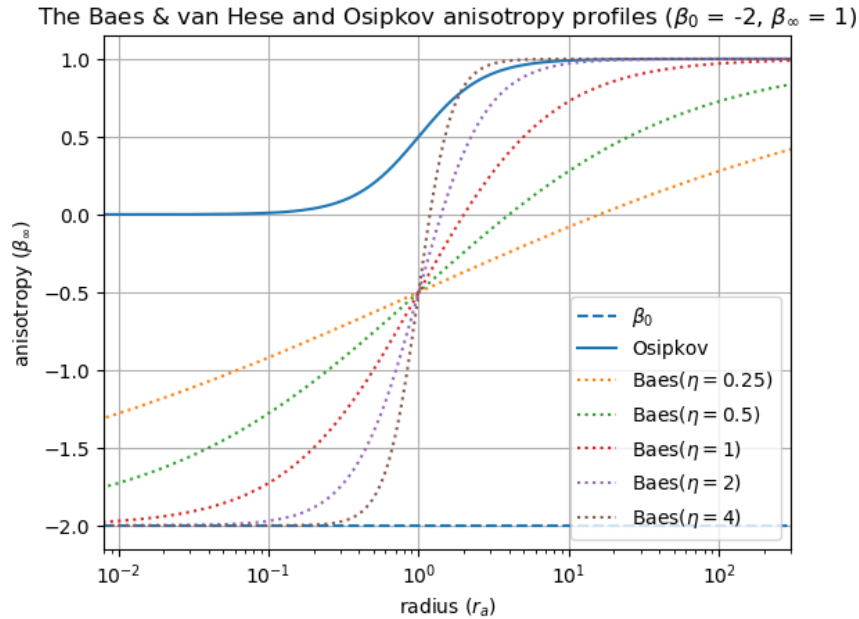
Figure 3.3: Three anisotropy profile types plotted. There are three distinguishing cases to consider: i) full isotropy ($\beta_{ani} = 0$), ii) radial isotropy ($\beta_{ani} = 1$) and iii) circular isotropy ($\beta_{ani} \to -\infty$). Note that $\beta_0 = 0, \eta = 2$ recovers the Osipkov profile from the Baes & van Hese profile.

3.3 Anisotropy profiles

Recall from Section 2 that the velocity dispersion anisotropy parameter is written in terms of $\beta_{ani} = 1 - \frac{\langle u_\varphi^2 \rangle}{\langle u_r^2 \rangle}$.
Such that $\beta_{ani} = 0$ corresponds with full isotropy and $\beta_{ani} = 1 \ (\to -\infty)$ with radial (circular) isotropy.
There are three variants used in the literature: a constant profile (3.10), the Osipkov-Merritt profile (3.11) and the Baes & van Hese profile (3.12) [14]. The Osipkov-Merritt profile yields 0 for $r \ll r_a$ and 1 for $r \gg r_a$, with r_a a scale radius. The last profile is the more general solution from which both the constant and Osipkov-Merritt profile can be regained, with β_0 and β_∞ the anisotropy at small and large radii, respectively.
However, the constant profile has been often used. This is primarily due to ease of computation, shortening the time to complete the fitting procedure. Due to the Mass-Anisotropy-Degeneracy, a change of anisotropy profile has a direct impact on the mass profile.

$$\beta_{ani}^{Cnst}(r) = \beta_0 \tag{3.10}$$

$$\beta_{ani}^{Osipkov}(r) = \frac{r^2}{r^2 + r_a^2} \tag{3.11}$$

$$\beta_{ani}^{Baes}(r) = \frac{\beta_0 + \beta_\infty (r/r_a)^\eta}{1 + \left(\frac{r}{r_a}\right)^\eta} \tag{3.12}$$

The difference between the constant and Osipkov-Merritt profiles is very large. By utilising the Baes & van Hese profile, both situations are taken in consideration. This is the profile as recommended by [14] because of its generality.

Note that the anisotropy profiles are linked to the light profiles aswell, as they must satisfy the *Global Density-Slope Anisotropy Inequality*[14, 21] This will be further discussed in Section 5.3.2.

4. Fitting Halo Parameters

With the possible profiles outlined in Section 3, we try to fit models for $\rho(r)$, $\beta_{ani}(r)$ and $I(R)$ to find ρ_{DM}. Note that up to 9 free parameters (Zhao-Hernquist and Baes & van Hese) have to be fitted.
A common method is to use Bayesian Analysis in combination with Monte Carlo methods, though there has been at least one fully frequentist approach defined [22].

4.1 Bayesian Parameter Inference

In order to quantify the knowledge we have, and the uncertainty thereof, we can make use of Bayesian Analysis. This revolves around an interpretation of Bayes' theorem (4.1).

$$P(\theta|D) = \frac{P(D|\theta) \cdot P(\theta)}{P(D)} \tag{4.1}$$

Here, $P(\theta)$ and $P(D)$ are the total probabilities of the parameters θ and the data D, with $P(D|\theta)$ the conditional probability of D given θ and $P(\theta|D)$ vice versa.

In Bayesian jargon, $P(\theta)$ is called the prior and $P(\theta|D)$ the posterior probability. They represent the confidence in your hypothesis before and after data has been taken into account. The $P(D|\theta)$ is then the likelihood of D given θ. This is where model specifics come into play. Note that in the following the term $P(D|\theta)$ will be notated by L for legibility.
Normal, independent and identically distributed data would get the following likelihood.

$$L = \prod_{i}^{n} P(x_i|\mu,\sigma) = \left(2\pi\sigma^2\right)^{-n/2} \exp\left(-\frac{1}{2\sigma^2}\sum_{i}^{n}(x_i - \mu)^2\right) \tag{4.2}$$

with μ and σ the parameters of the likelihood and x_i the data.

As $P(D)$ might involve many terms (possibly infinitely many) it is favourable to subdue its calculation. With certain techniques such as MLE (see Section 4.1.1) this is allowed, if $P(D)$ is not going to change. For example, this happens when keeping to the same measurement set. Thus giving rise to

$$P(\theta|D) \propto L(D|\theta) \cdot P(\theta)$$

Note that the choice for a certain prior $P(\theta)$ can introduce an artificial skewing of the posterior probability. This is especially clear when the prior has zeroes, as these can then never be developed. If there is no previous knowledge, a flat prior is chosen to sample all of the possible values.

4.1.1 Maximum Likelihood Estimation

One of the ways of fitting parameters to data in the Bayesian framework is called maximum likelihood estimation (MLE). It revolves around a postulated likelihood $L(x; \theta)$ of which the global maximum over the data x is sought by varying parameters θ.

This can be done on L itself, however, the log-likelihood $\mathcal{L} \equiv \log L$ is more often used for this. It is generally simpler to compute and, as the log function is monotonic, it has the same properties needed for the global maximum.

For example, taking the logarithm of (4.2) we get (4.3). We assumed independent and identically distributed data, so σ stays constant for each datapoint. This means the first term in (4.3) is a constant, so it can be dropped from the calculation when looking for the maximum of the likelihood.

$$\mathcal{L} = \log L = -\frac{n}{2} \log(2\pi\sigma^2) - \frac{1}{2\sigma^2} \sum (x_i - \mu)^2 \tag{4.3}$$

Defining the likelihood requires knowledge of the probability density functions of the parameters. However, these probability density functions are not always fully known or are too complex to calculate explicitly. There are methods to sample from such probability density functions using Monte Carlo methods.

4.1.2 Monte Carlo techniques

Monte Carlo techniques are a way of integrating or simulating quantities using (pseudo-)random numbers. It is especially powerful as a multi-dimensional integrator. The standard way of integrating a 1D function known as Riemann summing, works on an interval $[a, b]$ by splicing it into N parts. If we want to know the expectation value of the function f, equalling the geometrical average, it will correspond to

$$\langle f \rangle = \frac{1}{N} \sum_{i=1}^{N} f(x_i) \cdot (x_i - x_{i-1}). \tag{4.4}$$

However, on higher dimensional grids, this becomes cumbersome as the size of the pointset increases exponentially with the dimension of the grid.

Instead of Riemann summation we can use Monte Carlo methods to integrate numerically. The advantage of Monte Carlo integration versus deterministic methods, is that you can get a result at a fixed cost (the calculation of N points), eventhough the result deteriorates when increasing the dimensionality. This can be seen in

$$\langle f \rangle = \frac{1}{N} \sum_{i=1}^{N} f(\vec{x_i}), \tag{4.5}$$

where the x_i have been generated from a distribution $\mathcal{P}$ which might be somewhat tailored to the function f. In general, $\mathcal{P}$ is taken to be the uniform distribution on the wanted interval. There is also an estimator for the variance with

$$\sigma^2(f) = \langle f^2 \rangle - \langle f \rangle^2 = \frac{1}{N} \left(\sum_{i=1}^{N} f^2(\vec{x_i}) - \left[\sum_{i=1}^{N} f(\vec{x_i}) \right]^2 \right). \tag{4.6}$$

Note that the variance goes as $1/\sqrt{N}$, regardless of how many dimensions there are. This can be contrasted to other methods which generally have a variance that grows with increasing dimension.

4.2 Setting up the likelihood

Computing the ρ_{DM} of a dwarf galaxy involves fitting measured line-of-sight velocities u_i. One can posit a likelihood based on the line-of-sight velocity like (4.7). Assuming the velocities to be normally distributed (4.2) around an average velocity $\langle u \rangle$, [23] defines the likelihood as

$$L = \prod_{i=1}^{N_{stars}} \left[\frac{1}{\sqrt{2\pi}} \frac{1}{\sqrt{\sigma_p^2(R_i) + \Delta_{u_i}^2}} \exp\left(-\frac{1}{2}\left(\frac{u_i - \langle u \rangle}{\sqrt{\sigma_p^2(R_i) + \Delta_{u_i}^2}} \right)^2 \right) \right]^{P_i} . \tag{4.7}$$

In (4.7), the total velocity dispersion at R_i consists of a term indicating the measurement uncertainty on the velocity Δ_{u_i}, and the intrinsic projected dispersion $\sigma_p(R_i)$ as defined in (2.18). So $\sigma_p(R_i)$ is in fact the model to be fitted consisting of the profiles for ρ_{DM}, $I(R)$ and β_{ani}.

For each star, a factor P_i describes the probability that it belongs to the dwarf in question instead of it being contamination (that is to say, a fore- or background star). This weighting is not yet often used, corresponding to the binary class of $P_i = 0$ for stars not to be taken into account and $P_i = 1$ for those that should. Examples of the impact of taking wrong stars into account can be seen in Figure 4.1.
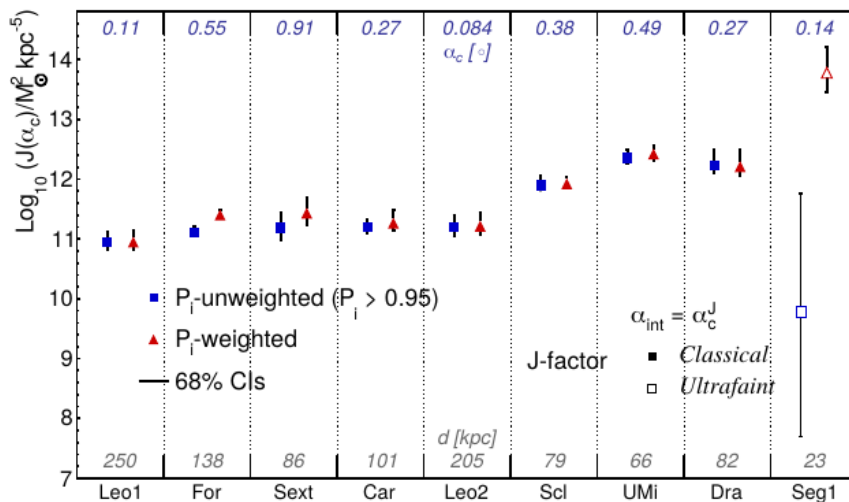
Figure 4.1: From [23]: J-factors for dwarf Spheroidal galaxies where membership probabilities are available. The red triangles correspond to using the membership probabilities. The blue rectangles are only stars with $P_i > 0.95$.

4.2.1 Numerical Maximum Likelihood Estimation

The full calculation of the combination of (4.7) and (2.18) with the profiles from Section 3 consists of multiple integrations and derivatives. The maximum likelihood is then difficult to find analytically.
Instead, one can try to estimate the maximum likelihood numerically. By specifying ranges for the different parameters we create a parameter space. Then, for various points in this space, we calculate the likelihood and pick the highest likelihood from the set.

Setting up the distribution in which parameters may vary has an influence on the ability to find the maximum. This distribution can put a bias in the calculation by putting emphasis on one region while neglecting to incorporate another area in the Monte Carlo computation.

To this end, such a distribution should, if possible, be physically motivated, or be as least informative as it can be. For the latter situation, as mentioned earlier, a common choice is taking a flat distribution. In Table 4.1, parameter distributions are listed as used by some authors.

Table 4.1: Priors as listed in the various papers. The minimal value for $\log_{10}(r_{-2})$ by [23] is because of the Global Density-Slope Anisotropy Inequality (see Section 5.3.2).

Paper	Profile	Parameter	Range
[23]	Einasto(3.3)	$\log_{10}(\rho_{-2})$	$[5, 13]$
		$\log_{10}(r_{-2})$	$[\log_{10}(r_s^*), 1]$
	Baes & van Hese(3.12)	β_0	$[-9, 1]$
		β_∞	$[-9, 1]$
		$\log_{10}(r_a)$	$[-9, 1]$
		η	$[0.1, 4]$
[13]	Zhao-Hernquist(3.4)	$\log(\rho_s)$	$[-4, +4]$
		$\log(r_s)$	$[0, +5]$
		α	$[0.5, 3]$
		β	$[3, 10]$
		γ	$[0, 1.2]$
	Constant Anisotropy(3.10)	$-\log_{10}(1 - \beta_a)$	$[-1, +1]$

4.3 Calculating the J-value

The use of MLE allows to find likely models for the halo profile parametrisations (ρ_{DM}, ν and β_{ani}). The J-value can then be calculated for each of the obtained mass density profiles by employing 1.2.
However, uncertainties on these values are not provided by this calculation. This means that they have to be determined in a different manner

Within the MLE framework, the concept of uncertainty is expressed in terms of credibility intervals. For an estimated parameter θ^{est}, the $1 - \alpha$ credibility interval (CI) is the interval containing the true parameter θ^{true} with a probability of α.
Using the Central Limit Theorem, one can show that the error $\mathcal{E}$ between the true parameter θ^{true} and the estimated parameter θ^{est}, is asymptotically normal distributed for many estimated parameters.

The models obtained by the MLE are estimated parameters and can therefore be used to determine this normal distribution. The mean μ and standard deviation σ of this distribution then determine the $1 - \alpha$ CI for θ as

$$\theta^{\pm(1-\alpha)CI} = \mu \pm \sqrt{\frac{\sigma}{n}} \left| z_{\frac{\alpha}{2}} \right| \tag{4.8}$$

where n is the number of models and $z_{\frac{\alpha}{2}}$ is the normal quantile function.

Regular uncertainty propagation can be used to determine the CI on a variable that depends on the determined parameters θ. This means that only the intervals of the mass density profile are propagated into the CIs on the J-value.

5. Constraining the J-value

To be able to give better limits on the particle physics factor ϕ_J^{PP} from (1.1) we can either improve the measured γ-ray signal or tie down uncertainties on the J-value. In Section 4 the J-value and its uncertainty have been calculated. But there are both systematic and random uncertainties to look into for constraining the J-value.

In this Section we first look into the dwarf galaxies to which the previously mentioned approach is applied as there are some differences between the dwarfs to be taken into account. Afterwards, the assumptions made for setting up the spherical Jeans equation are considered. At the end of this Section, the ways to decrease uncertainties from the likelihood calculation are explored.

5.1   Dwarf Galaxies

The reason for looking to dwarf galaxies for annihilation or decay signals is the high mass-to-light ratio Υ, expecting the discrepancy to be explained by dark matter. However, this comes with the price of having less light to observe as these systems commonly have less stars than a full-sized galaxy. This impacts the amount of stars that can be used as tracers for the velocity dispersion. But it also impacts the amount of stars to fit the light profile to.

Another factor is the amount of confirmed dwarf galaxies. At the turn of the century, only a few dwarfs were known, correspondingly known as classical dSphs. For these galaxies the number of sample stars is relatively high with $N \sim 1000$.[24]
Since then, the Dark Energy Survey (DES) collaboration has identified new dwarfs, among which are a new class of dSphs, Ultra Faint dSphs (UFDs)[25]. These dwarfs have a very low surface brightness and do not have that many sample stars, $N \sim 30$ [14].

It is important to distinguish between a dwarf galaxy and globular clusters. Globular clusters are reckoned to have no dark matter content [3]. Meanwhile, they are easily mistaken for a dwarf galaxy as they share approximately the same magnitudes. This can be seen in Figure 5.2, where some known globular clusters and dwarf galaxies are shown.
Differentiating between the globular clusters and the dwarf galaxies seems to be possible by finding distances and half-light radii of the object and determining the metallicities and ages of star populations.
The latter two are especially important as dwarf galaxies are expected to come from a cosmic origin, meaning that there should be populations that are old (> 10 Gyr) and have a low metallicity.
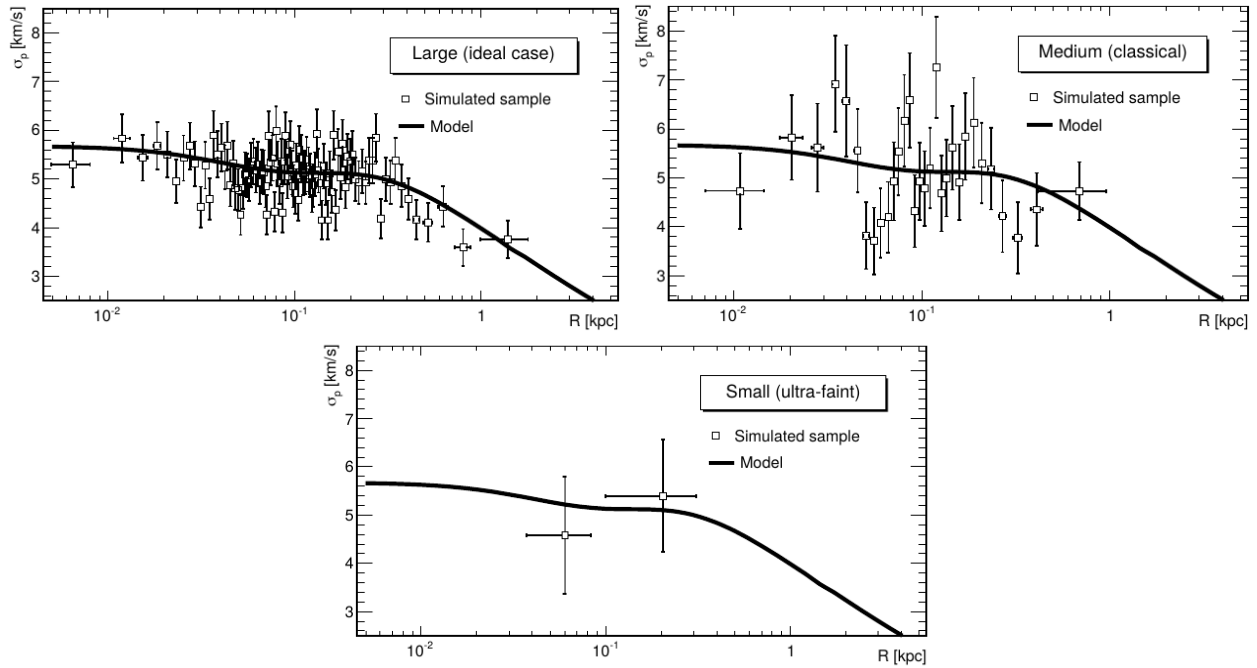
Figure 5.1: From [14]: "Velocity dispersion profile obtained for 3 sample sizes of a same model. *Left*: large sample, ideal case with 10000 stars. *Right*: medium sample, 1000 stars, corresponding to a classical dSph. *Bottom*: small sample, with 30 stars, mimicking an ultra-faint dSph."
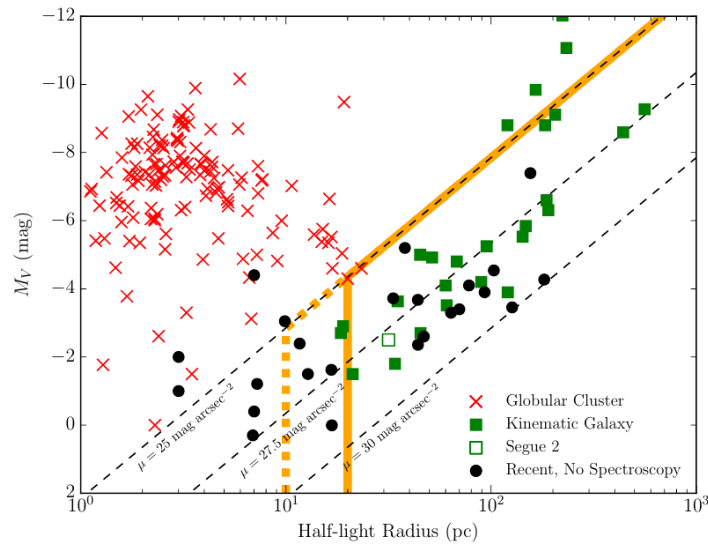
Figure 5.2: From [3]: "Absolute visual magnitude (M_V) versus physical half-light radius ($r_{1/2}$) for dSphs and globular clusters. Globular clusters, which do not contain measurable DM within their visible stellar distribution, are marked with red crosses. Spectroscopically confirmed DM-dominated dSphs are labeled with green squares. Segue 2 (open green square) has the chemical signature of a dSph, but exhibits a low velocity dispersion, and is therefore excluded from their target list. Milky Way satellites lacking spectroscopic observations are labeled with black filled circles. Thick orange lines indicate their target sample selection cuts on objects lacking spectroscopic data."

5.2   Violation of Spherical Symmetry

The most important assumptions we have made in Section 2.3 are hydrodynamical equilibrium and spherical symmetry. As a first order limit this works quite well. However, each of them can be violated to differing degrees.

For some dwarf galaxies, data indicates they are undergoing tidal interactions, thus ruling out strict hydrodynamical equilibrium. This is the case for Boötes III, Willman 1 and Tucana III [3]. One should therefore be cautious using these for the most stringent limits.

On a larger scale, the spherical symmetry is found to be questionable. All dwarfs exhibit elliptical rings of constant light called isophotes. This implies a violation of sphericity.[14]
We can loosen the assumption of spherical symmetry by introducing triaxiality. In effect, this requires us to redo the analysis of models and likelihood with a new geometry for the various distributions,

$$r_e = \sqrt{\left(\frac{x}{a}\right)^2 + \left(\frac{y}{b}\right)^2 + \left(\frac{z}{c}\right)^2}, \tag{5.1}$$

where x, y and z are cartesian coordinates aligned to the dwarf galaxy's frame.

Instead of merely using a new radius, we might set up the Jeans equation in an axisymmetric form. This is a well-studied scenario in e.g. [24, 26]. We take the same assumptions as used in Section 2.3 except for spherical symmetry, and assume the distribution function to be of the form $f(E, L_z)$, depending on the total energy E and angular momentum L_z. This last premise gives us a form of the Collisionless Boltzmann Equation in which the mixed moments are zero. This helps overall in rewriting to a new coordinate system as mentioned in Section 2.2.4.
Just as in Section 2.3.1, projection effects come into play. These projection effects will, however, not require computation of integrals such as required for the Abel transforms, making them faster to compute. The Collisionless Boltzmann Equation and Jeans equations corresponding with cylindrical coordinates can be found in Appendix A.4.

5.3   Optimizing the Likelihood calculation

Instead of changing the parametric models, or extending them to an axisymmetric case, the likelihood calculation itself might be optimised.
Some properties are expected to be shared across the population of dwarfs. By fitting these properties across the population, these observables can be better constrained.
The introduction of appropriate choices for priors can, in a similar manner, accomplish a better result.

5.3.1   Multi Level Hierarchical Modelling

Instead of determining each galaxy on its own accord, an underlying structure common to the dwarfs can be assumed. To effect this, multi level hierarchical model (MLM) can be used. In Martinez [5], MLM is outlined and applied as such, splitting properties of the dwarfs into two groups.
The first level consists of the usual individual dSph observables: line-of-sight velocities, metallicities, the position of stars and the total luminosity of the galaxy. The second level contains halo properties of the whole set of galaxies. For example, this contains slope parameters to the mass density profile ρ_{DM}.

5.3.2   Optimal cuts

Another method to optimise the likelihood calculation and its result is by choosing the priors (as used in Section 4.2.1) carefully. By limiting a prior, we influence both the confidence intervals and the obtained value.

According to [14], an important cut can be made on the integration angle α_{int} used for integrating the mass density to obtain the J-value using Equation (1.2). Standard choices for this angle are the angle corresponding to the outermost star fitted, α_{max}, and an angle of 0.5°. [14, 27] suggest a critical value of $\alpha_c \approx 2\frac{r_{1/2}}{d}$ comparing the half light radius with the distance to the dwarf, where the half light radius is independent of the light profile in use. As can be seen in Figure 5.3, this critical value maximises the J-value while at the same time minimising its uncertainty.
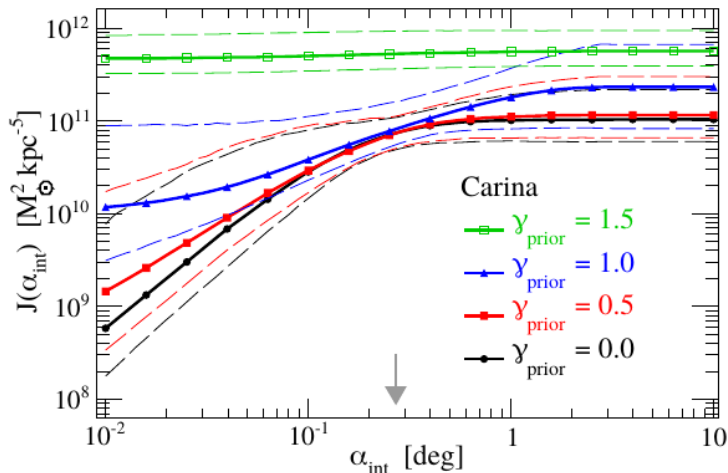
Figure 5.3: From Walker et al. [27]: J median value and 95% CLs from four independent Markov Chain Monte Carlo analyses of the Carina dwarf galaxy, keeping the 'core' parameter γ fixed at the indicated values. The arrow identifies $\alpha_{int} = \alpha_c$.

By imposing another cut on the mass density's scaling radius r_s, Bonnivard et al. [14] finds that taking this scaling radius to be at least as large as the half light radius (see Table 4.1) helps in reducing the uncertainties on the J-value (see Figure 5.4). In their analysis of mock data, the Markov Chain Monte Carlo (MCMC) estimator is improved finding a median value closer to the true value, combined with smaller uncertainties.

A third constraint to acknowledge, mentioned in Section 3.3, is the Global Density-Slope Anisotropy In-equality (5.2) [21]. In rough terms, the maximum attainable anisotropy is determined by the slope of the stellar number density. The constraint is necessary as it ensures that the phase space distribution function $f(\vec{w}, t)$ introduced in Section 2.1 stays positive. Thus, it provides a degree of safety against non-physical solutions to the Jeans equation [14].

$$\beta_{ani} \leq -\frac{1}{2}\frac{\mathrm{d}\log\nu(r)}{\mathrm{d}\log r} \tag{5.2}$$
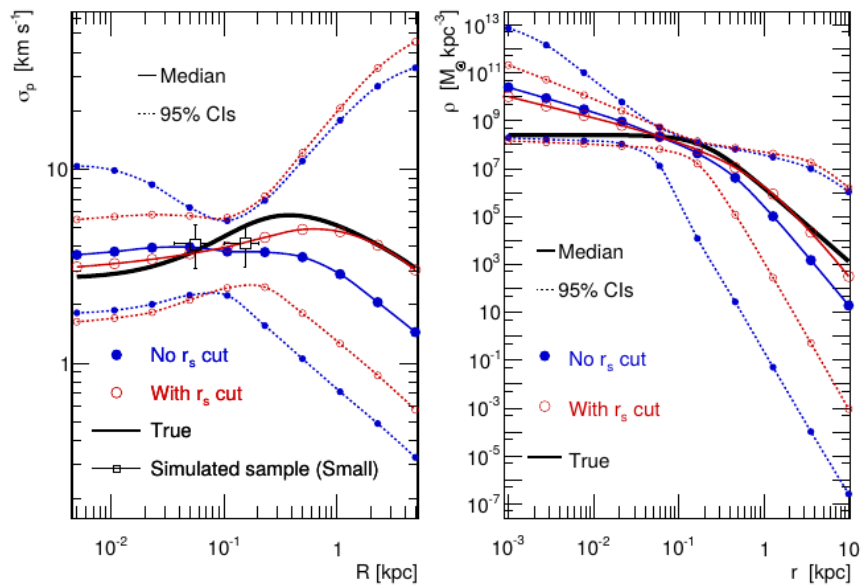
Figure 5.4: From [14]: "Median values (solid lines with symbols) and 95% CLs (thin dashed lines with symbols) for the velocity dispersion profile (left) and the DM density profile (right). Enforcing the condition $r_s > r_s^*$ (red empty circles compared to blue filled circles) in the prior of the MCMC analysis (see Table 1) lead to better results, i.e. with the median value closer to the true value with smaller uncertainties (less biased and better estimator). The model shown corresponds to a mock ultra-faint dSph galaxy with $\gamma = 0$, $r_s = 0.2$kpc and $r_s^* = 0.1$kpc."

6. Conclusion

Dark matter is theorised to consist of Weakly Interacting Massive Particles. The examination of γ-ray radiation from dwarf galaxies around the Milky Way and kinematical analyses of these dwarfs, made possible by spectroscopic measurements, allow to set limits on the dark matter particle.
One such type of kinematical analysis is called Jeans analysis. It relates measurements from multiple stars to cope with missing components to the position and velocity vectors of these stars by averaging a phasespace density function.

In this document, Jeans analysis and parametric methods, used for its computation, are explored to obtain the dwarf galaxy's mass density function. By integrating the square of the mass density function, a characteristic value called J-value is calculated for a dwarf. Joint with the γ-ray spectrum, this J-value is used to set the previously mentioned constraints.

The Jeans analysis requires the introduction of quantities such as velocity dispersion anisotropy and surface brightness. These quantities are cast in a parametric form and, if possible, related to observationally accessible quantities. As there are multiple parametrisations to choose from, some common models, as used in the literature, are outlined. While outlining, differences between models are analysed and recommendations made on picking an applicable model.

The computation of the Jeans equation requires performing both integrals and derivatives. Inverting the equation is analytically hard to accomplish, so numerical methods are used to find the optimal parameters. The parameters are allowed to change according to a prior distribution. By fitting each set of parameters and comparing the resulting fits to each other, these optimal parameters can be found.

Some further techniques and considerations can be taken into account for minimising uncertainties and maximising the obtained limits. Examples of such are Multi-Level Modelling to incorporate an underlying model shared between the dwarf galaxies for the determination of the mass density function, and the introduction of Triaxiality into both the Jeans analysis and the parametric models.

In Table 6.1, various effects on the uncertainty of the J-value are listed. These effects include choosing a wrong parametric models for the velocity dispersion anisotropy β_{ani} and light profile I^{light}. Another effect listed is the similarity of Zhao and Einasto mass density profiles when applied to dwarf spheroidal galaxies.

	Annihilation			**Decay**			**Comments**
	Ultra-faint	*Classical*	*Ideal*	*Ultra-faint*	*Classical*	*Ideal*	
Bias from:	$J^{median}/J^{true}(\alpha_c^J)$			$D^{median}/D^{true}(\alpha_c^D)$			
Einasto vs Zhao	none	none	none	none	none	none	$\rightarrow$ use Einasto + cuts‡
Wrong β_{ani}	none	$\lesssim 3$	$\lesssim 10$	none	$\lesssim 2.5$	$\lesssim 2$	$\rightarrow$ use $\beta_{ani}^{\mathrm{Baes}}$
Wrong I^{light}	$\lesssim 2$	$\lesssim 3$	$\lesssim 3$	$\lesssim 1.5$	$\lesssim 4$	$\lesssim 4$	$\rightarrow$ use Zhao
Triaxiality	$\lesssim 2.5$	$\lesssim 2.5$	$\lesssim 2.5$	$\lesssim 2$	$\lesssim 2$	$\lesssim 2$	Systematic uncertainty
Uncertainties†;	$J^{\pm95\%CL}/J^{median}(\alpha_c^J)$			$D^{\pm95\%CL}/D^{median}(\alpha_c^D)$			
Maximum knowledge	$\lesssim 20$	$\lesssim 2$	$\lesssim 1.5$	$\lesssim 8$	$\lesssim 1.5$	$\lesssim 1.25$	DM only + cuts‡
$\rho_{DM}^{\mathrm{Einasto}} + \beta_{ani}^{\mathrm{Baes}}$ modelling	$\lesssim 20$	$\lesssim 4$	$\lesssim 2.5$	$\lesssim 10$	$\lesssim 2$	$\lesssim 2$	

‡Enforce $r_s \geq r_s^*$ and $\alpha \geq 0.12$ in the priors.

†Light profile uncertainties have a very small effect on J and D at α_c, and are not shown here.

Table 6.1: Table 4 from [14]: "Summary of all effects discussed in the paper for annihilation and decay (J and D-factors). The upper block corresponds to biases induced by the choices of parametrisation and halo triaxiality. The lower block gives the minimum (*maximum knowledge*) and typical ($\rho_{DM}^{\mathrm{Einasto}} + \beta_{ani}^{\mathrm{Baes}}$ modelling) uncertainties expected in a data-driven Jeans analysis. Note that we show the quantity $J^{\pm95\%CL}/J^{median}$ instead of $J^{\pm95\%CL}/J^{true}$, in order to be comparable to the expectations of real data analyses."

A. Various equations

A.1 Liouville equation of $\rho(p, q; t)$:

$$\frac{d\rho}{dt} = \frac{\partial \rho}{\partial t} + \sum_{i=1}^{n} \left(\frac{\partial \rho}{\partial q_i} \frac{\partial q_i}{\partial t} + \frac{\partial \rho}{\partial p_i} \frac{\partial p_i}{\partial t} \right) = 0 \qquad \text{(A.1.1)}$$

A.2 Euler's equation for fluids with pressure p and density ρ

$$\rho \frac{\partial v}{\partial t} + \rho \left(v \cdot \nabla \right) v = \rho \nabla \Phi - \nabla p \qquad \text{(A.2.1)}$$

A.3 Abel transforms

$$\text{Projecting:} \quad F(r) = \quad 2 \int_{r}^{\infty} f(s) \frac{s \, ds}{\sqrt{s^2 - r^2}} \qquad \text{(A.3.1a)}$$

$$\text{Deprojecting:} \quad f(s) = -\frac{1}{\pi} \int_{s}^{\infty} \frac{dF}{dr} \frac{dr}{\sqrt{r^2 - s^2}} \qquad \text{(A.3.1b)}$$

A.4 Cylindrical and Spherical CBE and Jeans equations

Cylindrical (r, θ, z) $\qquad\qquad$ Collisionless Boltzmann Equation

$$\frac{\partial f}{\partial t} + u_r \frac{\partial f}{\partial r} + \frac{u_\theta}{r} \frac{\partial f}{\partial \theta} + u_z \frac{\partial f}{\partial z} + \left(\frac{u_\theta^2}{r} - \frac{\partial \Phi}{\partial r} \right) \frac{\partial f}{\partial u_r} + \left(-\frac{u_r u_\theta}{r} - \frac{1}{r} \frac{\partial \Phi}{\partial \theta} \right) \frac{\partial f}{\partial u_\theta} - \frac{\partial \Phi}{\partial z} \frac{\partial f}{\partial u_z} = 0 \qquad \text{(A.4.1)}$$

First Moment

$$\int \frac{df}{dt} \, d^3u = \frac{\partial \nu}{\partial t} + \frac{\partial \left(\nu \langle u_r \rangle \right)}{\partial r} + \frac{1}{r} \frac{\partial \left(\nu \langle u_\theta \rangle \right)}{\partial \theta} + \frac{\partial \left(\nu \langle u_z \rangle \right)}{\partial z} + \frac{\nu}{r} \langle u_r \rangle = 0 \qquad \text{(A.4.2)}$$

Radial Second Moment

$$\int u_r \frac{df}{dt} \, d^3u = \frac{\partial \nu \langle u_r \rangle}{\partial t} + \frac{\partial \left(\nu \langle u_r^2 \rangle \right)}{\partial r} + \frac{1}{r} \frac{\partial \left(\nu \langle u_\theta u_r \rangle \right)}{\partial \theta} + \frac{\partial \left(\nu \langle u_z u_r \rangle \right)}{\partial z} + \nu \left(\frac{\langle u_r^2 \rangle - \langle u_\theta^2 \rangle}{r} + \langle \frac{\partial \Phi}{\partial r} \rangle \right) = 0 \quad \text{(A.4.3)}$$

Radial Jeans Equation

$$\int u_r \frac{df}{dt} \, d^3u - \langle u_r \rangle \int \frac{df}{dt} \, d^3u = \nu \frac{\partial \langle u_r \rangle}{\partial t} + \frac{\partial \left(\nu \sigma_{rr}^2 \right)}{\partial r} + \frac{1}{r} \frac{\partial \left(\nu \sigma_{r\theta}^2 \right)}{\partial \theta} + \frac{\partial \left(\nu \sigma_{rz}^2 \right)}{\partial z} + \nu \langle \frac{\partial \Phi}{\partial r} \rangle$$
$$+ \nu \left(\frac{1}{r} \langle u_\theta \rangle \frac{\partial \langle u_r \rangle}{\partial \theta} + \langle u_r \rangle \frac{\partial \langle u_r \rangle}{\partial r} + \langle u_z \rangle \frac{\partial \langle u_r \rangle}{\partial z} + \frac{\sigma_r^2 - \langle u_\theta^2 \rangle}{r} \right) = 0 \quad \text{(A.4.4)}$$

Spherical (r, φ, θ) Collisionless Boltzmann Equation

$$\frac{\partial f}{\partial t} + u_r \frac{\partial f}{\partial r} + \frac{u_\varphi}{r \sin \theta} \frac{\partial f}{\partial \varphi} + \frac{u_\theta}{r} \frac{\partial f}{\partial \theta} + \left(\frac{u_\theta^2 + u_\varphi^2}{r} - \frac{\partial \Phi}{\partial r} \right) \frac{\partial f}{\partial u_r}$$

$$+ \left(\frac{-u_r u_\varphi - u_\varphi u_\theta \cot \theta}{r} - \frac{1}{r \sin \theta} \frac{\partial \Phi}{\partial \varphi} \right) \frac{\partial f}{\partial u_\varphi} + \left(\frac{u_\varphi^2 \cot \theta - u_r u_\theta}{r} - \frac{1}{r} \frac{\partial \Phi}{\partial \theta} \right) \frac{\partial f}{\partial u_\theta} = 0 \quad \text{(A.4.5)}$$

First Moment

$$\int \frac{\mathrm{d}f}{\mathrm{d}t} \, \mathrm{d}^3 u = \frac{\partial \nu}{\partial t} + \frac{\partial \left(\nu \langle u_r \rangle \right)}{\partial r} + \frac{1}{r} \frac{\partial \left(\nu \langle u_\theta \rangle \right)}{\partial \theta} + \frac{1}{r \sin \theta} \frac{\partial \left(\nu \langle u_\varphi \rangle \right)}{\partial \varphi} = 0 \quad \text{(A.4.6)}$$

Radial Second Moment

$$\int u_r \frac{\mathrm{d}f}{\mathrm{d}t} \, \mathrm{d}^3 u = \frac{\partial \left(\nu \langle u_r \rangle \right)}{\partial t} + \frac{\partial \left(\nu \langle u_r^2 \rangle \right)}{\partial r} + \frac{1}{r} \frac{\partial \left(\nu \langle u_\theta u_r \rangle \right)}{\partial \theta} + \frac{1}{r \sin \theta} \frac{\partial \left(\nu \langle u_\varphi u_r \rangle \right)}{\partial \varphi} - \nu \left(\frac{\langle u_\theta^2 \rangle + \langle u_\varphi^2 \rangle - \langle u_r^2 \rangle}{r} - \langle \frac{\partial \Phi}{\partial r} \rangle \right) = 0$$

$$\text{(A.4.7)}$$

Jeans Equation

$$\int u_r \frac{\mathrm{d}f}{\mathrm{d}t} \, \mathrm{d}^3 u - \langle u_r \rangle \int \frac{\mathrm{d}f}{\mathrm{d}t} \, \mathrm{d}^3 u = \nu \frac{\partial \langle u_r \rangle}{\partial t} + \frac{\partial \left(\nu \sigma_{rr}^2 \right)}{\partial r} + \frac{1}{r} \frac{\partial \left(\nu \sigma_{r\theta}^2 \right)}{\partial \theta} + \frac{1}{r \sin \theta} \frac{\partial \left(\nu \sigma_{r\varphi}^2 \right)}{\partial \varphi} - \nu \left(\frac{\langle u_\theta \rangle^2 + \langle u_\varphi^2 \rangle - \langle u_r^2 \rangle}{r} - \langle \frac{\partial \Phi}{\partial r} \rangle \right)$$

$$+ \langle u_r \rangle \frac{\partial \left(\nu \langle u_r \rangle \right)}{\partial r} + \frac{\langle u_r \rangle}{r} \frac{\partial \left(\nu \langle u_\theta \rangle \right)}{\partial \theta} + \frac{\langle u_r \rangle}{r \sin \theta} \frac{\partial \left(\nu \langle u_\varphi \rangle \right)}{\partial \varphi} = 0 \quad \text{(A.4.8)}$$

Bibliography

[1] Alan W. McConnachie. "The observed properties of dwarf galaxies in and around the Local Group". In: *Astron. J.* 144 (2012), p. 4. DOI: 10.1088/0004-6256/144/1/4. arXiv: 1204.1562 [astro-ph.CO].

[2] J. D. Simon et al. "Stellar Kinematics and Metallicities in the Ultra-Faint Dwarf Galaxy Reticulum II". In: *Astrophys. J.* 808.1 (2015), p. 95. DOI: 10.1088/0004-637X/808/1/95. arXiv: 1504.02889 [astro-ph.GA].

[3] Fermi-LAT. "Searching for Dark Matter Annihilation in Recently Discovered Milky Way Satellites with Fermi-LAT". In: *Astrophys. J.* 834.2 (2017), p. 110. DOI: 10.3847/1538-4357/834/2/110. arXiv: 1611.03184 [astro-ph.HE].

[4] Alex Geringer-Sameth, Savvas M. Koushiappas, and Matthew G. Walker. "Comprehensive search for dark matter annihilation in dwarf galaxies". In: *Phys. Rev.* D91.8 (2015), p. 083535. DOI: 10.1103/PhysRevD.91.083535. arXiv: 1410.2242 [astro-ph.CO].

[5] Gregory D. Martinez. "A robust determination of Milky Way satellite properties using hierarchical mass modelling". In: *Mon. Not. Roy. Astron. Soc.* 451.3 (2015), pp. 2524–2535. DOI: 10.1093/mnras/stv942. arXiv: 1309.2641 [astro-ph.GA].

[6] Joe Wolf. "Modeling mass independent of anisotropy". In: *IAU Symp.* 271 (2011), p. 110. DOI: 10.1017/S1743921311017510. arXiv: 1009.0295 [astro-ph.CO].

[7] Julio F. Navarro, Carlos S. Frenk, and Simon D. M. White. "The Structure of cold dark matter halos". In: *Astrophys. J.* 462 (1996), pp. 563–575. DOI: 10.1086/177173. arXiv: astro-ph/9508025 [astro-ph].

[8] A. Burkert. "The Structure of dark matter halos in dwarf galaxies". In: *IAU Symp.* 171 (1996). [Astrophys. J.447,L25(1995)], p. 175. DOI: 10.1086/309560. arXiv: astro-ph/9504041 [astro-ph].

[9] Ben Moore et al. "Cold collapse and the core catastrophe". In: *Mon. Not. Roy. Astron. Soc.* 310 (1999), pp. 1147–1152. DOI: 10.1046/j.1365-8711.1999.03039.x. arXiv: astro-ph/9903164 [astro-ph].

[10] J. Einasto. "On the Construction of a Composite Model for the Galaxy and on the Determination of the System of Galactic Parameters". In: *Trudy Astrofizicheskogo Instituta Alma-Ata* 5 (1965), pp. 87–100.

[11] Alister W. Graham et al. "Empirical models for Dark Matter Halos. I. Nonparametric Construction of Density Profiles and Comparison with Parametric Models". In: *Astron. J.* 132 (2006), pp. 2685–2700. DOI: 10.1086/508988. arXiv: astro-ph/0509417 [astro-ph].

[12] H. Zhao. "Analytical models for galactic nuclei". In: *Monthly Notices of the Royal Astronomical Society* 278.2 (Jan. 1996), pp. 488–496. DOI: 10.1093/mnras/278.2.488. URL: https://doi.org/10.1093/mnras/278.2.488.

[13] Alex Geringer-Sameth, Savvas M. Koushiappas, and Matthew Walker. "Dwarf galaxy annihilation and decay emission profiles for dark matter experiments". In: *Astrophys. J.* 801.2 (2015), p. 74. DOI: 10.1088/0004-637X/801/2/74. arXiv: 1408.0002 [astro-ph.CO].

[14] V. Bonnivard et al. "Spherical Jeans analysis for dark matter indirect detection in dwarf spheroidal galaxies - Impact of physical parameters and triaxiality". In: *Mon. Not. Roy. Astron. Soc.* 446 (2015), pp. 3002–3021. DOI: 10.1093/mnras/stu2296. arXiv: 1407.7822 [astro-ph.HE].

[15] E. Retana-Montenegro et al. "Analytical properties of Einasto dark matter haloes". In: *Astron. Astrophys.* 540 (2012), A70. DOI: 10.1051/0004-6361/201118543. arXiv: 1202.5242 [astro-ph.CO].

[16] A. Agnello and N. W. Evans. "A Virial Core in the Sculptor Dwarf Spheroidal Galaxy". In: *Astrophys. J.* 754 (2012), p. L39. DOI: 10.1088/2041-8205/754/2/L39. arXiv: 1205.6673 [astro-ph.GA].

[17] A. Del Popolo and F. Pace. "The Cusp/Core problem: supernovae feedback versus the baryonic clumps and dynamical friction model". In: *Astrophys. Space Sci.* 361.5 (2016). [Erratum: Astrophys. Space Sci.361,no.7,225(2016)], p. 162. DOI: 10.1007/s10509-016-2820-2,10.1007/s10509-016-2742-z. arXiv: 1502.01947 [astro-ph.GA].

[18] Antonino Del Popolo et al. "Energy transfer from baryons to dark matter as a unified solution to small-scale structure issues of the CDM model". In: (2018). DOI: 10.1103/PhysRevD.98.063517. arXiv: 1809.10609.

[19] J. An and H. Zhao. "Fitting functions for dark matter density profiles". In: *Mon. Not. Roy. Astron. Soc.* 428 (2013), pp. 2805–2811. DOI: 10.1093/mnras/sts175. arXiv: 1209.6220 [astro-ph.CO].

[20] H. C. Plummer. "On the Problem of Distribution in Globular Star Clusters: (Plate 8.)" In: *Monthly Notices of the Royal Astronomical Society* 71.5 (Mar. 1911), pp. 460–470. DOI: 10.1093/mnras/71.5.460. URL: https://doi.org/10.1093/mnras/71.5.460.

[21] Luca Ciotti and Lucia Morganti. "How general is the global density slope-anisotropy inequality?" In: *Mon. Not. Roy. Astron. Soc.* 408 (2010), p. 1070. DOI: 10.1111/j.1365-2966.2010.17184.x. arXiv: 1006.2344 [astro-ph.CO].

[22] A. Chiappo et al. "Dwarf spheroidal J-factors without priors: A likelihood-based analysis for indirect dark matter searches". In: *Mon. Not. Roy. Astron. Soc.* 466.1 (2017), pp. 669–676. DOI: 10.1093/mnras/stw3079. arXiv: 1608.07111 [astro-ph.CO].

[23] V. Bonnivard et al. "Dark matter annihilation and decay in dwarf spheroidal galaxies: The classical and ultrafaint dSphs". In: *Mon. Not. Roy. Astron. Soc.* 453.1 (2015), pp. 849–867. DOI: 10.1093/mnras/stv1601. arXiv: 1504.02048 [astro-ph.HE].

[24] Kohei Hayashi et al. "Dark matter annihilation and decay from non-spherical dark halos in galactic dwarf satellites". In: *Mon. Not. Roy. Astron. Soc.* 461.3 (2016), pp. 2914–2928. DOI: 10.1093/mnras/stw1457. arXiv: 1603.08046 [astro-ph.GA].

[25] A. Drlica-Wagner et al. "Eight Ultra-faint Galaxy Candidates Discovered in Year Two of the Dark Energy Survey". In: *Astrophys. J.* 813.2 (2015), p. 109. DOI: 10.1088/0004-637X/813/2/109. arXiv: 1508.03622 [astro-ph.GA].

[26] James Binney and Scott Tremaine. *Galactic Dynamics*. 2nd ed. Princeton Press, 1987. ISBN: 9780691084459.

[27] M. G. Walker et al. "Dark matter in the classical dwarf spheroidal galaxies: a robust constraint on the astrophysical factor for gamma-ray flux calculations". In: *Astrophys. J.* 733 (2011), p. L46. DOI: 10.1088/2041-8205/733/2/L46. arXiv: 1104.0411 [astro-ph.HE].